Applied Catalysis B: Environmental 158–159 (2014) 348–354

Contents lists available at ScienceDirect

Applied Catalysis B: Environmental

journal homepage: www.elsevier.com/locate/apcatb

Highly active and CO_2 tolerant Ir nanocatalysts for H_2/CO_2 separation in electrochemical hydrogen pumps

Soo Jin Kim[a,b], Hee-Young Park[a], Sang Hyun Ahn[a], Byung-seok Lee[a,b], Hyoung-Juhn Kim[a], EunAe Cho[a], Dirk Henkensmeier[a], Suk Woo Nam[a], Sung Hyun Kim[b,***], Sung Jong Yoo[a,**], Jong Hyun Jang[a,*]

[a] Fuel Cell Research Center, Korea Institute of Science and Technology (KIST), Seoul 136-791, Republic of Korea
[b] Department of Chemical and Biological Engineering, Korea University, Seoul 136-701, Republic of Korea

ARTICLE INFO

Article history:
Received 16 December 2013
Received in revised form 10 March 2014
Accepted 8 April 2014
Available online 30 April 2014

Keywords:
Electrochemical hydrogen pump
Gas separation
Carbon capture and storage
Iridium catalyst
CO_2 stripping

ABSTRACT

Carbon-supported Pt nanoparticles have been widely used as electrocatalysts for electrochemical hydrogen pumps. However, Pt surfaces are susceptible to poisoning under CO_2 atmosphere, and as a result, need greater applied cell voltages. Instead of Pt as an anode catalyst in electrochemical hydrogen pumps, we synthesized Ir-based catalysts and characterized them by XRD, XPS, TEM, and TGA. The electrochemical characteristics of the Ir catalysts were evaluated by a halfcell test, and their catalytic activities toward the hydrogen oxidation and hydrogen evolution reactions were evaluated by micro polarization analysis. The exchange current density of the Ir catalyst that was heat treated at 300 °C was larger than that of commercial Pt. CO_2 stripping analysis confirmed that the Ir catalyst was not affected by CO_2, unlike the Pt catalyst. Focusing on H_2 separation from H_2/CO_2 gas, an evaluation using a single-cell test indicated that the Ir catalyst performed better than the Pt catalyst.

© 2014 Elsevier B.V. All rights reserved.

1. Introduction

The rapid increase in atmospheric CO_2 concentration is considered to be a causative factor in global climate change. Therefore, various technologies have been developed to increase the energy efficiency of fossil-fuel based systems (e.g., hybrid electric vehicles) and to replace conventional systems (e.g. solar cells and wind power). In addition, CO_2 capture and storage (CCS) technologies have been actively researched and developed [1,2]. As CO_2 sources usually produce mixtures that contain other gases such as H_2 and H_2O, gas separation technologies are required to increase the efficiency of CCS processes.

As an alternative to conventional gas separation technologies such as pressure swing adsorption (PSA) and temperature swing adsorption (TSA), the electrochemical hydrogen pump is expected to be effectively utilized for H_2/CO_2 gas separation. When electrical power is supplied to an electrochemical hydrogen pump, the hydrogen oxidation reaction (HOR) and hydrogen evolution reaction (HER) occur at the anode and cathode, respectively. Then, hydrogen gas is transported through proton exchange membranes (PEM) in the form of protons, where the transport rate is directly proportional to the current density (Scheme 1). Similar to PEM-based fuel cells (PEMFC), electrochemical hydrogen pumps can be fabricated with perfluorosulfonic acid membranes [3–10] and phosphoric acid-doped polybenzimidazole membranes [11–13]. Electrochemical hydrogen pumps will be suitable for the treatment of gas mixtures produced from coal gasification and steam-reforming processes [14,15], as well as the anode outlet gases from molten carbonate fuel cells integrated with fossil fuel power plants [16].

As electrocatalysts for electrochemical hydrogen pumps, carbon-supported Pt nanoparticles have been widely used for hydrogen compression [5,9,11] and hydrogen separation from gas mixtures [3,4,6–8,11–13]. However, it was reported that, under CO_2 atmosphere, Pt surfaces can be poisoned by the strong adsorption of CO molecules that are generated through the reverse water-gas shift reaction of CO_2 and adsorbed hydrogen [17]. Therefore, when H_2/CO_2 gas mixtures are supplied to electrochemical hydrogen pumps, the Pt catalyst in the anodes can be largely deactivated, necessitating increased applied cell voltages. Pt poisoning by very small amount of CO has been previously reported [4], whereas

* Corresponding author. Tel.: +82 2 958 5287; fax: +82 2 958 5199.
** Corresponding author. Tel.: +82 2 958 5260; fax: +82 2 958 5199.
*** Corresponding author. Tel.: +82 2 3290 3297; fax: +82 2 926 6102.
E-mail addresses: kimsh@korea.ac.kr (S.H. Kim), ysj@kist.re.kr, snupeel@gmail.com (S.J. Yoo), jhjang@kist.re.kr (J.H. Jang).

http://dx.doi.org/10.1016/j.apcatb.2014.04.016
0926-3373/© 2014 Elsevier B.V. All rights reserved.

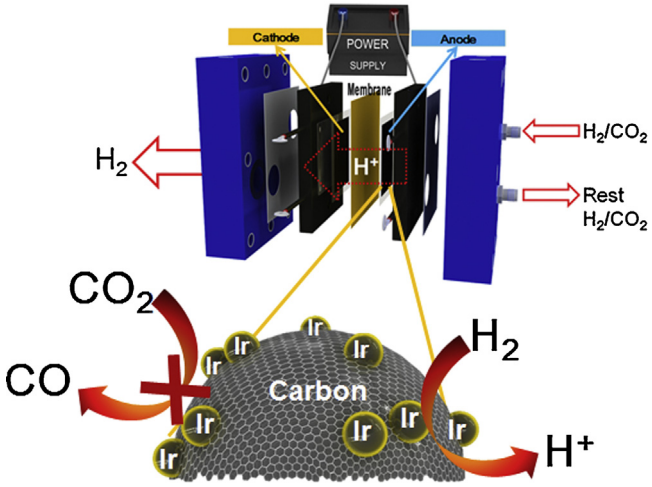

Scheme 1. Schematic diagram of electrochemical hydrogen pump.

only dilution effect have been observed when hydrogen feed was mixed with Ar [10], N_2 [8,12], and CH_4 [3]. For example, Onda et al. reported that the applied voltage for H_2 separation was significantly larger for a H_2/CO_2 mixture (127 mV at 0.05 A cm^{-2}) compared to that for a H_2/Ar mixture (66 mV) [8], indicating Pt deactivation under the CO_2 atmosphere.

In this study, for the application of hydrogen separation from CO_2-rich mixture gas, Ir-based catalysts were synthesized as candidate anode catalysts for electrochemical hydrogen pumps, and their electrochemical characteristics were investigated by half-cell and single-cell tests, focusing on poisoning under CO_2 atmosphere. Even though Rh and Pd metals have HOR activities comparable to Pt catalysts [18,19], poisoning under CO_2 atmosphere has been reported to be much smaller for Ir surfaces [20] compared to Rh [21] and Pd [22]. Therefore, for H_2 separation from rich CO_2 gas mixtures, the Ir-based electrocatalysts are expected to provide good performance with significantly decreased material cost, compared to conventional Pt electrocatalysts [2].

2. Experimental

2.1. Materials

Iridium (III) chloride hydrate ($IrCl_3{\cdot}xH_2O$), ethylene glycol (EG, <99%), sodium hydroxide (NaOH), sulfuric acid (H_2SO_4, 95–98%), and perchloric acid ($HClO_4$, 70%) were purchased from Sigma–Aldrich. Nafion® perfluorinated resin solution (Nafion, 5 wt%) was purchased from Aldrich and isopropyl alcohol (IPA, 99.99%) was purchased from Burdick & Jackson. Carbon black (Vulcan® XC-72R) was purchased from Cabot Corporation and the carbon-supported platinum catalyst (Pt, HISPEC 3000, 20 wt%) was purchased from Alfa Aesar. Nafion® 212 membrane was purchased from DuPont. Sigracet® 10BC with a microporous layer (MPL) was purchased from SGL Carbon, Inc.

2.2. Preparation of iridium catalysts

Catalyst preparation involved two stages, in which IrO_x nanoparticles were first impregnated on carbon (IrO_x/C), followed by heat treatment at different temperatures under reducing conditions to generate Ir nanoparticles on carbon (Ir/C). For the first stage, $IrCl_3{\cdot}xH_2O$ (0.3 g) was refluxed in a three-necked flask at 100 °C for 1 h under Ar atmosphere and then allowed to cool naturally. Separately, carbon black (0.1 g) was dispersed in DI water (600 mL) through ultrasonic vibration and magnetic stirring. An adequate amount of the IrO_x colloid was added to the carbon dispersion to obtain a 15 wt% IrO_x/C mixture. After 30 min of vigorous stirring, 2 M H_2SO_4 (300 mL) was slowly added to the mixture. After stirring overnight, the solids were filtered and dried in an oven at 60 °C. IrO_x/C was then reduced to Ir/C in a tube furnace by flowing H_2 gas for 2 h at a flow rate of 100 mL min^{-1} and at varying temperatures (200, 250, and 300 °C) to form the Ir/C nanoparticles [23].

2.3. Characterization methods

Thermogravimetric analysis (TGA) was performed under air atmosphere, scanning up to 800 °C at a heating rate of 10 °C min^{-1} (TGA Q50, TA Instruments). X-ray diffraction (XRD) analysis was carried out with a Cu Kα source (λ = 1.541 Å) at 30 kV and 15 mA (MiniFlex II, Rigaku), where 2θ was scanned from 20° to 90° at a scan rate of 0.1° min^{-1}. The electronic structures of the catalysts were investigated by means of X-ray photoelectron spectroscopy (XPS; PHI-5000 Versaprobe, ULVAC-PHI Inc.). Deconvolutions of the XPS spectra were carried out using the XPS Peak 4.1 program. After the backgrounds are determined using the Shirley function, the peak positions are determined through curve fitting using mixed Gaussian–Lorentzian line shapes. Relative concentrations of the surface species are equal to the corresponding area ratio (deconvoluted peak area divided by the total XPS signal area extracted from the experimental XPS spectras). Catalyst surfaces were examined by transmission electron microscopy (TEM; Tecnai-20, FEI Corp.). Samples were prepared by placing a drop of the catalyst solution onto a copper grid and then drying.

2.4. Half-cell test

The half-cell test was conducted using a glassy carbon electrode (5 mm diameter) as a working electrode, a saturated calomel electrode (SCE, 3 M KCl) as a reference electrode, and a platinum wire as a counter electrode. A catalyst ink was prepared by mixing catalyst (10 mg), IPA (1 mL), and 5 wt% Nafion (100 μL). The catalyst ink was dropped on the glassy carbon electrode and dried. All electrochemical measurements were carried out at 5 °C (PGSTAT 302N, Eco Chemie). Polarization curves of the hydrogen oxidation reaction (HOR) and hydrogen evolution reaction (HER) were obtained using a rotating disk electrode (RDE) in saturated H_2 at 3000 rpm with a 1 mV s^{-1} scan rate. After holding the potential at 0.35 V vs. RHE for 15 min and 0.05 V vs. RHE for 15 min while with purging with CO_2, cyclic voltammograms were obtained under saturated Ar at potentials of 0.05–1.06 V vs. RHE at a scan rate 20 mV s^{-1} in 0.1 M $HClO_4$.

2.5. Single-cell test

The hydrogen pump experiment was carried out at a cell temperature of 70 °C using a test station (CNL Energy Co.). To the anode side, pure hydrogen, a gas mixture of H_2 (20%) and Ar (80%), and a gas mixture of H_2 (20%) and CO_2 (80%) were supplied at room temperature and 90% relative humidity (RH) at flow rates of 116, 584, and 584 mL min^{-1}, respectively. To the cathode side, pure hydrogen was supplied with 90% RH at a flow rate of 100 mL min^{-1} at room temperature. A potentiostat (HCP-803, Bio-Logic) was used to evaluate AC impedance spectra following each point on the polarization curve. Electrochemical impedance was measured at specified voltages from 0.05 to 0.5 V in potentiostatic mode. AC impedance measurements were carried out by applying an AC current perturbation to an electrochemical cell and measuring the potential response of the cell. *I–V* curves were determined as the voltage values measured for each current.

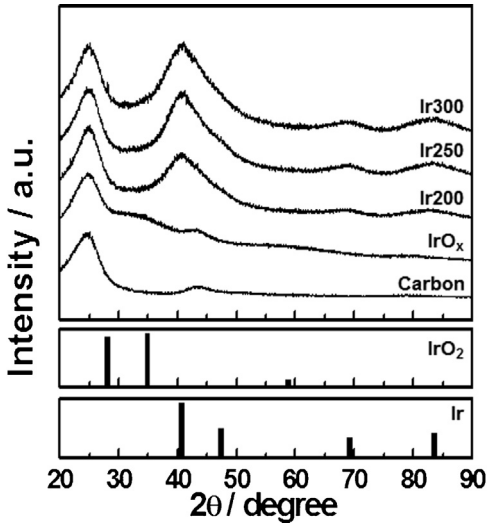

Fig. 1. XRD patterns of carbon (Vulcan XC-72), IrO_x, and Ir prepared at different heat-treatment temperatures (°C).

3. Results and discussion

3.1. Structural characterization

Fig. 1 shows the XRD spectra of the plain carbon substrate and synthesized Ir-based catalysts. In each sample, the carbon substrate peak was clearly observed at 24.8°. For the catalyst prepared without heat treatment, a broad peak appeared at around 31° which was assigned to overlapped signals from the (1 1 0) and (1 0 1) diffraction peaks of IrO_x, which has peak positions at 28° and 34°, respectively (JCPDS#65-2822). When the Ir-based catalysts were heat-treated under H_2 atmosphere, peaks developed at 40.8°, 68.8°, and 83.2°, which correspond to the (1 1 1), (2 0 0), and (3 1 1) diffractions of metallic Ir nanoparticles (JCPDS#65-9327). Thus, the as-prepared and heat-treated catalysts were identified as IrO_x/C and Ir/C, respectively. The Ir-based catalysts were designated as Ir200, Ir250, and Ir300 according to the heat-treatment temperature (°C).

The effect of heat treatment on the oxidation states was analyzed by XPS; the Ir 4f spectra are shown in Fig. 2. For IrO_x, the Ir $4f_{7/2}$ and Ir $4f_{5/2}$ peaks appear at 62.2 and 65.3 eV (Table 1). When the iridium oxide is reduced by heat treatment (Ir200, Ir250, and Ir300), the XPS peaks shift to lower binding energies (61.4 and 64.4 eV) to indicate the formation of metallic Ir. The experimental Ir $4f_{7/2}$ binding energies of the Ir nanoparticles were slightly higher than the reported value for an iridium powder [24], which is in accordance with previous reports for the nanoparticle effect [25]. Compared with the Au $4f_{7/2}$ core-level photoemission spectrum of a bulk Au polycrystalline evaporated film, the photoemission spectrum of a corresponding Au nanoparticle (2.6 nm) shifted to higher energy (0.45 eV). This is the result of the Coulomb interaction between the photoelectrons and photo-holes during the photoemission process and the nanoparticle substrate interaction.

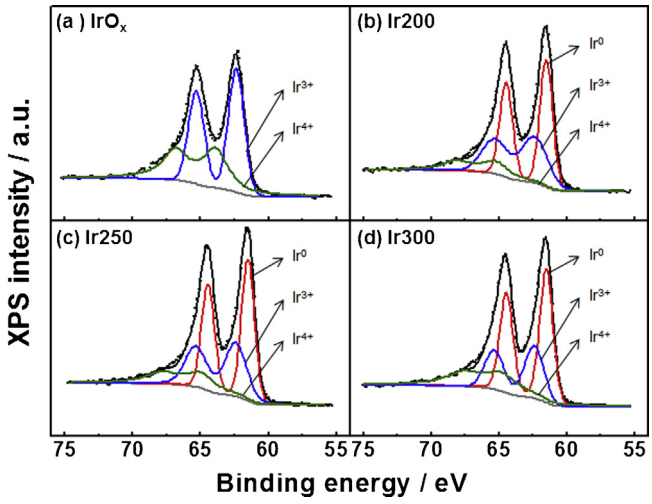

Fig. 2. XPS spectra of 4f levels for IrO_x and Ir prepared at different heat-treatment temperatures (°C).

Table 1
Binding energies of Ir $4f_{7/2}$ electrons for Ir catalysts and area ratio.

$Ir4f_{7/2}$	Oxide state	Binding energy (eV)	Area ratio (%)
	Ir^0	–	
IrO_x	Ir^{3+}	62.4	58.7
	Ir^{4+}	63.9	41.3
	Ir^0	61.5	49.5
Ir200	Ir^{3+}	62.4	36.3
	Ir^{4+}	63.9	14.2
	Ir^0	61.5	49.7
Ir250	Ir^{3+}	62.4	33.6
	Ir^{4+}	63.9	16.7
	Ir^0	61.5	49.9
Ir300	Ir^{3+}	62.4	27.1
	Ir^{4+}	64.8	22.9

Fig. 3 compares the TEM images of a commercial Pt catalyst and the synthesized IrO_x and Ir catalysts. From each image, the diameters of about 100 particles were measured and an average diameter was determined. The average diameter of the prepared IrO_x nanoparticles was 2.1 nm, which is comparable to that of the commercial Pt/C (2.0 nm). In the case of the heat-treated catalysts, the population of larger nanoparticles gradually increased with temperature, as shown in the histograms (insets); therefore, the average particle size also increased (2.0 nm (Ir200), 2.1 nm (Ir250), and 2.4 nm (Ir300)). From the particle diameter data set, the surface areas of the particles were summed to give the total surface area, and the total mass was determined by summing the mass of each particle. Spherical nanoparticles were assumed in these calculations. Then, the total surface area was divided by the total mass to give the specific surface area (SSA) for each catalyst with non-uniform size. We noted that the electrochemically active surface area, that is conventionally utilized for Pt nanoparticles was not applicable to the Ir-based catalysts. The SSA gradually decreased with higher heat treatment temperature (126.84 $m^2\,g^{-1}$ (Ir200), 118.53 $m^2\,g^{-1}$ (Ir250), and 102.04 $m^2\,g^{-1}$ (Ir300)). The SSA of the commercial Pt/C (125.91 $m^2\,g^{-1}$) was comparable to the Ir-metal catalysts. In the case of the synthesized IrO_x catalyst, the SSA was as high as 234.6 $m^2\,g^{-1}$, due to its lower specific density (IrO_2: 11.66 g cm^{-3}) compared to Ir (22.65 g cm^{-3}) and Pt (21.09 g cm^{-3}).

The Ir-based catalysts were analyzed by TGA to determine the IrO_x or Ir loading (Fig. 4). Initially, water evaporation was observed up to 200 °C at a scan rate of 10 °C min^{-1}, and a gradual weight decrease due to the decomposition of the carbon substrate was measured between 300 and 600 °C. Then, for the as-prepared catalyst, the IrO_x loading could be determined to be 17.4 wt%, directly from the residual weight at 600 °C, which corresponds to an Ir amount of 14.8 wt%. For the metallic Ir catalysts, a weight increase through oxide formation during the TGA analysis should be considered, as Ir metal can be oxidized at ca. 400 °C under air atmosphere [26]. For example, the residual weight of Ir200 (16.3 wt%) was converted to the Ir metal weight (14.3 wt%), simply based on the molecular weights of IrO_x and Ir. Similarly, the Ir metal loadings were determined to be 14.6 and 15 wt% for Ir250 and Ir300, respectively.

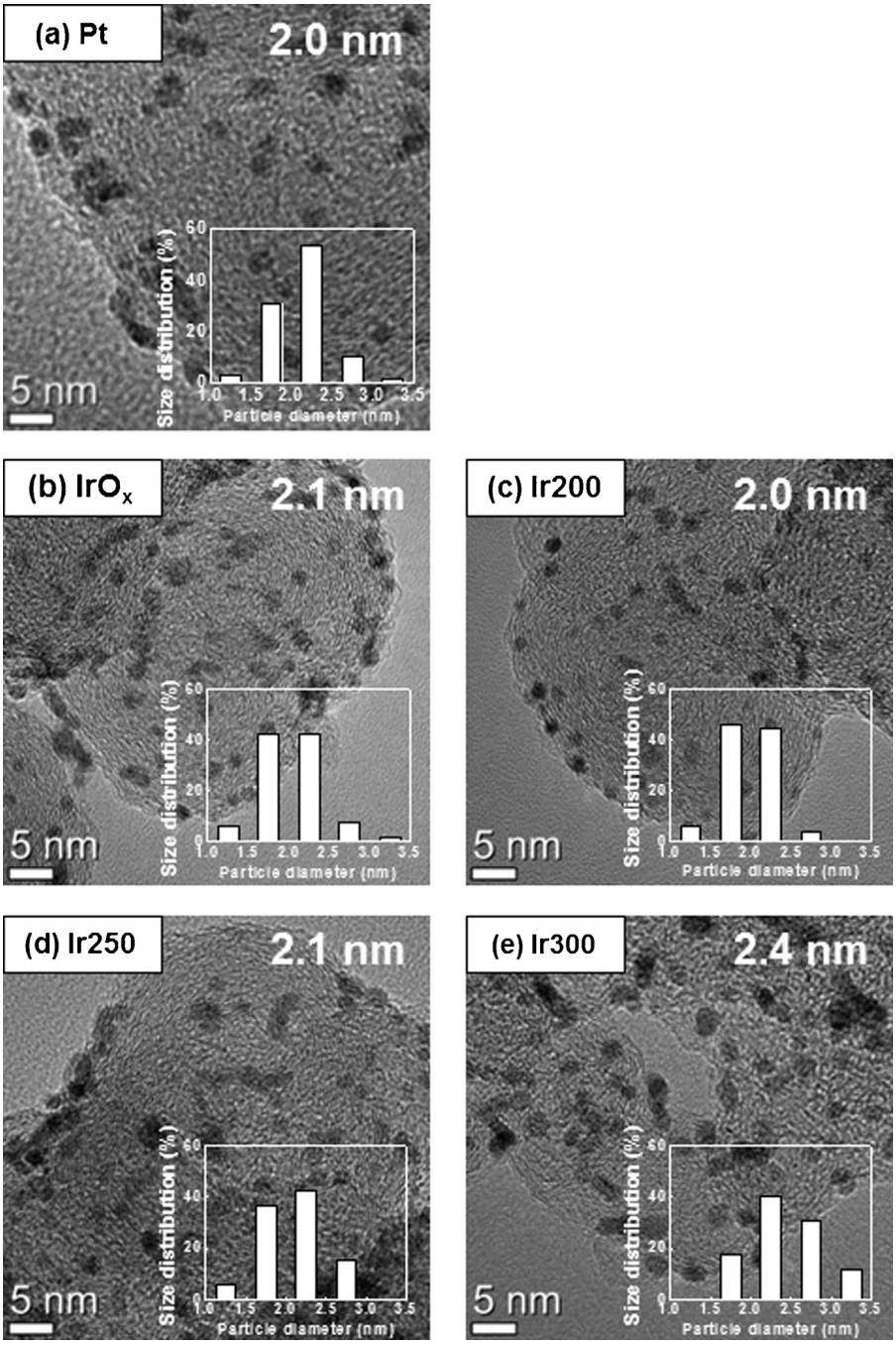

Fig. 3. TEM images and size distribution of catalysts: (a) Pt; (b) IrO_x; (c) Ir200 (heat treatment at 200 °C for 2 h); (d) Ir250 (heat treatment at 250 °C for 2 h); and (e) Ir300 (heat treatment at 300 °C for 2 h).

3.2. Electrochemical measurements in the half-cell test

The catalytic activity toward HOR and HER was evaluated by micro polarization analysis (Fig. 5a) [27]. For each sample, the measured current (i) changed linearly with a small overpotential (η) with small variation (<10 mV), where HOR and HER were responsible for the positive and negative polarizations, respectively. As its slope was larger, the Ir300 was expected to provide higher HOR/HER activity than the commercial Pt catalyst. For each catalyst, 45 data points in the potential range between −10 and 10 mV were linearly fitted and the specific exchange current densities ($i_{0,sp}$) were calculated from the slopes: 51.2 A g^{-1} (Pt), 29.2 A g^{-1} (IrO_x), 45.2 A g^{-1} (Ir200), 46.7 A g^{-1} (Ir250), and 57.4 A g^{-1} (Ir300). For this, the following equation was utilized, where i is the measured current, m is the catalyst mass, F is the Faraday constant (96,485 °C mol^{-1}), R is the gas constant (8.314 J mol^{-1} K^{-1}), and T is the cell temperature (278.15 K in this study) [27].

$$\frac{i}{m} = \frac{F}{RT} \cdot i_{0,sp} \cdot \eta$$

Fig. 5b shows the exchange current density (i_0) which was calculated by dividing the specific exchange current density ($i_{0,sp}$) by the SSA from the TEM analysis. The activity of the reduced Ir nanoparticles gradually increased with heat-treatment temperature. The exchange current density of Ir300 (0.058 mA cm^{-2}) exceeded that of the commercial Pt nanoparticle catalyst

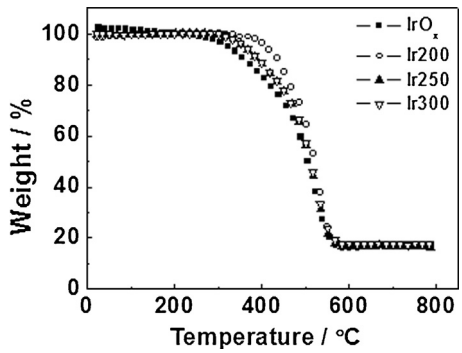

Fig. 4. TGA curves for IrO_x and Ir prepared at different heat-treatment temperatures (°C).

(0.042 mA cm^{-2}). Please note that the experimental i_0 of Pt/C in this study (particle size: 2.0 nm; 5 °C) was about 68% lower than the reported value of 0.134 mA cm^{-2} at 20 °C (particle size: 3.4 nm) [28], probably due to the combined effect of particle size and temperature. It was reported that, when the diameter of Pt nanoparticles was decreased from 3.3 to 2.6 nm, the exchange current density decreased by about 30% [29], and the activity on the Pt (1 0 0) plane was decreased by 34% with a temperature decrease from 30 to 1 °C [27].

For the Pt- and Ir-based catalysts, the CO_2 adsorption characteristics were examined by CO_2 stripping analysis (Fig. 6). It was reported that the Pt surface can be poisoned in the presence of CO_2 gas through the following chemical reaction, resulting in strong CO_2 reduction product (adsorbed CO) adsorption on the surface Pt atoms [30].

$$2Pt - H_{ad} + CO_2 \rightarrow Pt - CO_{ad} + H_2O + Pt$$

For experimental verification, while the electrode potential was fixed at 0.05 V vs. RHE, CO_2 gas was bubbled in the 0.1 M $HClO_4$ electrolyte solution for 15 min; then, the CO_2 dissolved in the electrolyte solution was removed by Ar purging for 15 min. When the

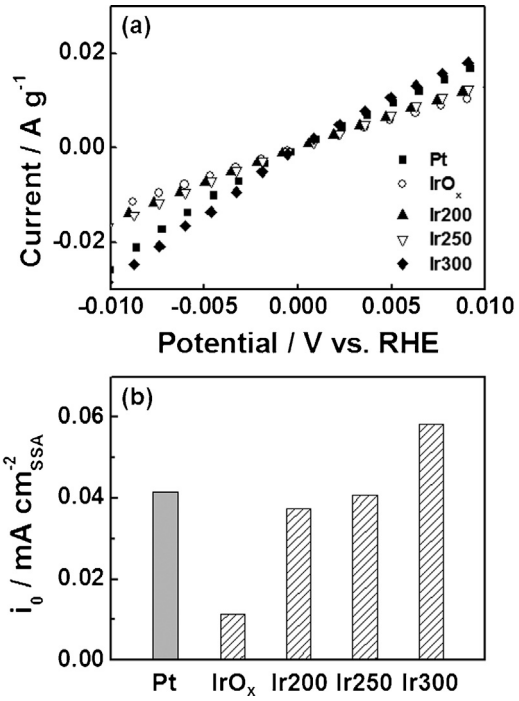

Fig. 5. (a) Micro-polarization of catalysts after H_2 saturation in 0.1 M $HClO_4$. (b) Exchange current densities of catalysts.

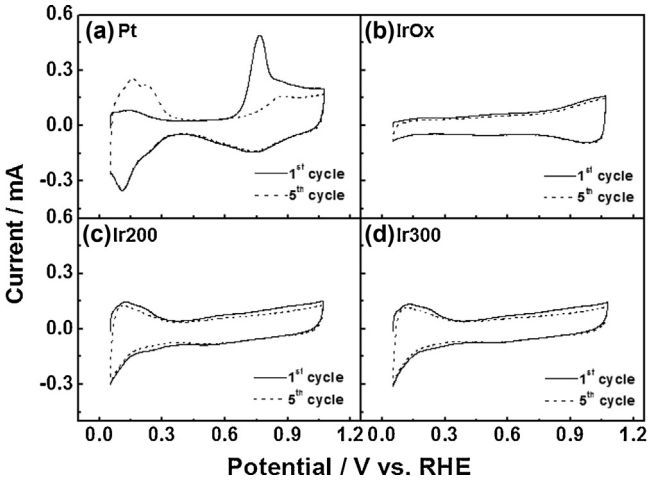

Fig. 6. Cyclic voltammetry after oxidation of reduced CO_2 in 0.1 M $HClO_4$ solution for (a) Pt, (b) IrO_x, (C) Ir200 (heat treatment at 200 °C for 2 h), and (d) Ir300 (heat treatment at 300 °C for 2 h).

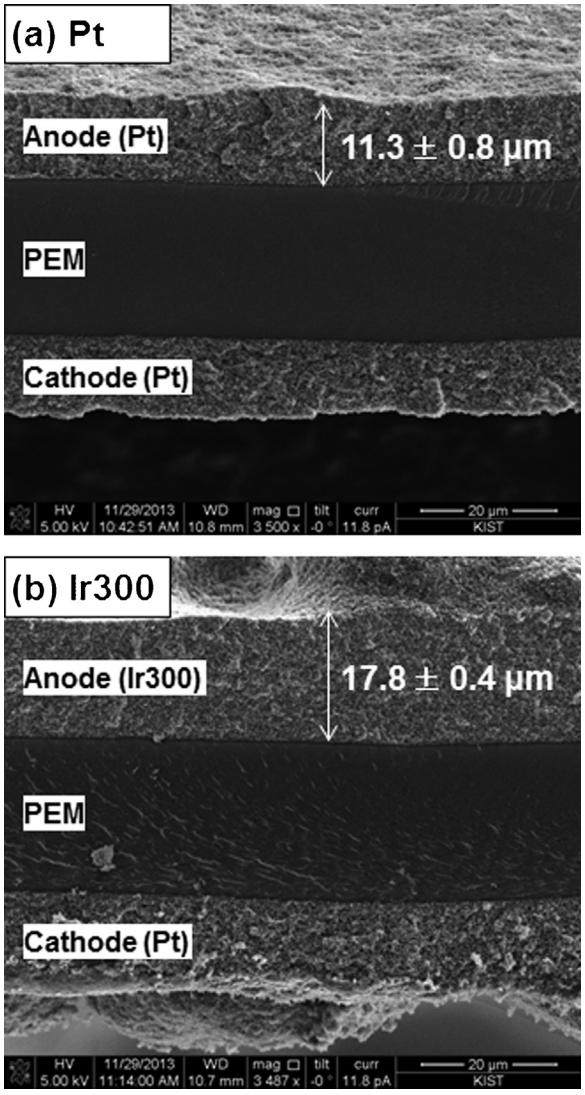

Fig. 7. Cross-sectional SEM images after operation at 70 °C for hydrogen pump MEAs of (a) Pt and (b) Ir300.

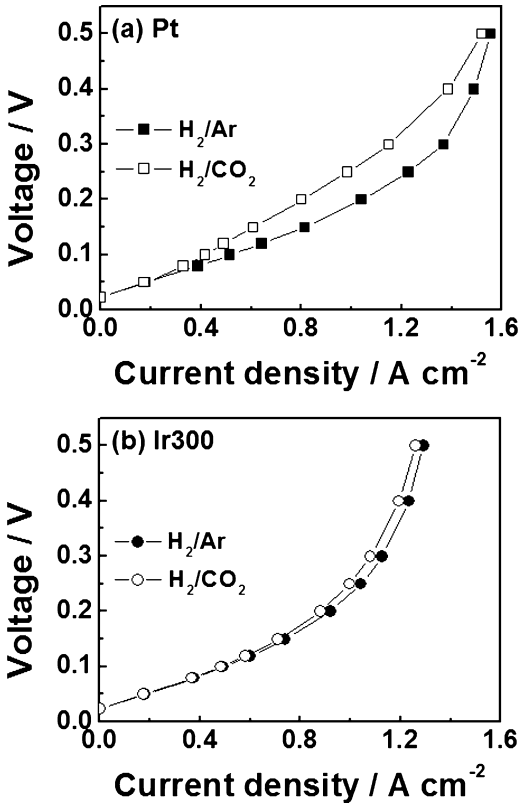

Fig. 8. Effects of (a) Pt (loading: 0.2 mg cm^{-2}) and (b) Ir300 (loading: 0.2 mg cm^{-2}) anodic catalysts on performance of electrodes at 70 °C with 584 mL min^{-1} H_2/Ar or H_2/CO_2.

electrode potential was swept anodically, an anodic peak from the electrochemical oxidation of the adsorbed CO molecules appeared clearly at ca. 0.78 V (Fig. 6a, solid line) [31]. Then, the electrode potential was cycled between 0.05 and 1.07 V vs. RHE and stabilized CV curves were obtained (5th cycle, dashed line in Fig. 6a), which showed that adsorbed CO molecules were totally removed from the catalyst surface.

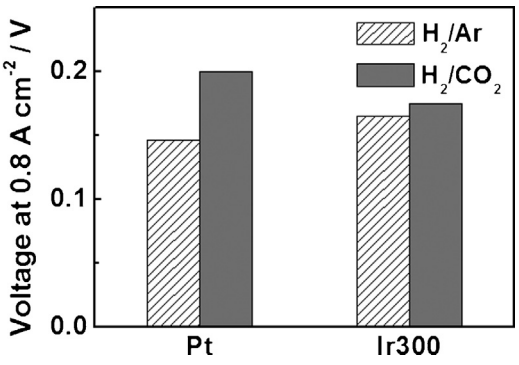

Fig. 9. Performance of electrochemical hydrogen pump at 0.8 A cm^{-2} and 70 °C with 584 mL min^{-1} H_2/Ar or H_2/CO_2.

For the Ir-based catalysts, very different characteristics were confirmed in the CO_2 stripping analysis. After an identical pretreatment to expose the Ir catalyst to CO_2, the electrochemical desorption of adsorbed CO was not observed, and therefore, there was no significant difference between the first (solid lines) and fifth (dashed lines) CV curves, which is in accordance with the previous report for Ir single crystals [20]. However, iridium does surffer CO gas poisoning [32]. Based on this, it can be confirmed that the reaction that converts CO_2 to CO did not readily proceed for the Ir-based catalysts, as compared to the Pt surface.

3.3. Electrochemical hydrogen pump performance for CO_2-rich feed mixture

Two membrane electrode assemblies (MEAs) were fabricated using Pt or Ir300 as the anode catalyst, and their hydrogen separation performance was characterized in the electrochemical hydrogen pump mode. The anode catalyst loading was fixed at 0.2 mg cm^{-2} for both the Pt and Ir300 catalysts. For the cathodes of both MEAs, a Pt catalyst was loaded at the same rate (0.2 mg cm^{-2}). Therefore, the cathode thickness was similar for the two MEAs: 12.6 ± 0.7 and 13.0 ± 0.5 μm for the Pt and Ir300 anode catalysts, respectively (Fig. 7). However, the anode thickness was much larger for the Ir300 anode (17.8 ± 0.4 μm) compared to the Pt anode

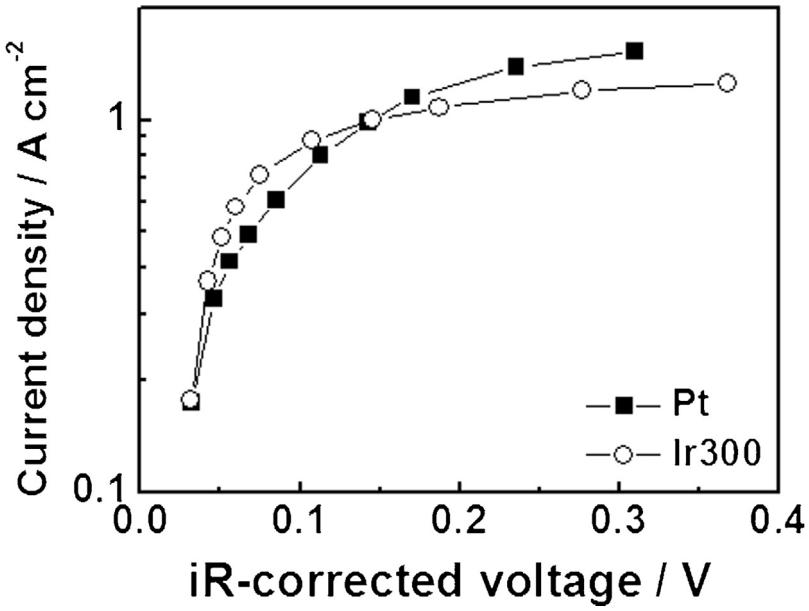

Fig. 10. Tafel plots of Pt and Ir300 at 70 °C with 584 mL min^{-1} H_2/CO_2.

($11.3 \pm 0.8\ \mu m$), due to the difference in the metal loading between the Pt (20 wt%) and Ir300 (15 wt%) electrocatalysts.

Fig. 8 shows the polarization curves for hydrogen separation from H_2/Ar (2:8) and H_2/CO_2 (2:8) gas mixtures. As the hydrogen fraction was fixed at 0.2, the effect of CO_2 could be accurately analyzed without a dilution effect. Then, the H_2 partial pressure during hydrogen pump operation would be higher at the cathode side (1 atm) compared to the anode side (0.2 atm). Accordingly, the open circuit voltage (OCV), based on the Nernst equation, was calculated to be 0.023 V, which is in good agreement with experimental OCV values. For the MEA with the Pt anode, the applied voltage with the H_2/Ar feed gradually increased as the H_2 separation rate increased (current increase). When the feed gas was changed to the H_2/CO_2 mixture, the voltage increase was clearly observed at current densities larger than $0.3\ A\ cm^{-2}$. This additional overpotential with a large amount of CO_2 can be explained by blocking of the Pt surface by CO, as discussed previously for Fig. 6. However, in the case of the MEA with the Ir300 anode, the voltage increase with the CO_2-rich feed was very small compared to the Pt anode, as shown in Fig. 8b. This clearly indicates that catalyst deactivation is much smaller on the Ir metal catalyst, where CO adsorption is not as severe as on the Pt surface.

Fig. 9 shows the applied voltage at $0.8\ A\ cm^{-2}$ for two MEAs with Pt and Ir300 electrocatalysts as the anodes. When the feed gas contains no CO_2 (H_2/Ar mixture), the operating voltage of the Pt anode (0.15 V) is smaller than that of the Ir300 anode (0.17 V). As the electrode thickness is larger for the Ir300 anode, it would seem that the mass transport limitation would be more severe, and influence the overall cell performance. When the feed gas was changed to the H_2/CO_2 mixture, the operating voltage with the Pt anode significantly increased, whereas the voltage increase for the MEA with the Ir300 anode was much smaller. As a result, the operating voltage to separate H_2 from the CO_2-rich feed was smaller for Ir300 (0.18 V) compared to the Pt-MEA (0.20 V). Therefore, it can be concluded that the Ir300 catalyst, which demonstrates good HOR activity and high CO_2 tolerance, can be effectively utilized as an anode catalyst in an electrochemical hydrogen pump. The Tafel plot in Fig. 10 also clearly shows that the Ir300 anode has higher catalytic activity under the H_2/CO_2 (2:8) mixture than the conventional Pt catalyst, even though the limiting current is lower for Ir300 with its thicker anode layer.

4. Conclusion

Ir/C electrocatalysts were prepared to compare their performance with a conventional Pt/C catalyst in H_2 recovery from H_2/CO_2 gas mixtures in an electrochemical hydrogen pump. The reduction of the as-prepared IrO_x catalyst to Ir(0) catalysts upon heat treatment at several temperatures under reducing conditions was confirmed by XRD and XPS analyses. Catalytic activities toward HOR and HER were evaluated by micro polarization analysis. The Ir300 catalyst ($0.059\ mA\ cm_{SSA}{}^{-2}$) demonstrated higher HOR/HER activity than the commercial Pt catalyst ($0.043\ mA\ cm_{SSA}{}^{-2}$). By CO_2 stripping analysis, an electrochemical desorption peak to remove adsorbed in situ generated CO from the catalyst surface was not observed for the Ir catalyst, unlike Pt (ca. 0.78 V). Accordingly, the Ir300 catalyst had good hydrogen oxidation activity and high CO_2 tolerance. The hydrogen separation performance of Pt and Ir300 was characterized in the electrochemical hydrogen pump mode. The operating voltage to separate H_2 from a H_2/CO_2 gas mixture was smaller for Ir300 (0.18 V at $0.8\ A\ cm^{-2}$), compared to the Pt-MEA (0.20 V at $0.8\ A\ cm^{-2}$). Therefore, for the separation of H_2 from a CO_2-rich gas mixture, the Ir-based electrocatalysts are expected to provide good performance with significantly decreased material costs, compared to the conventional Pt electrocatalysts.

Acknowledgements

This work was supported by the Korea CCS R&D Center (KCRC) grant funded by the Korea government (Ministry of Science, ICT & Future Planning) (No. 2013M1A8A1038315) and by the "COE (Center of Excellence)" program and Institutional Program (contract number 2E24841) of the Korea Institute of Science and Technology. SJY acknowledge financial support by the Global Frontier R&D Program on Center for Multiscale Energy System funded by the National Research Foundation under the Ministry of Science, ICT & Future, Korea (No. 2012M3A6A7054283).

References

[1] IEA, Pathways to a Clean Energy System, International Energy Agency, 2012.
[2] S. Satyapal, M. Mills, S. Byham, Z. Hou, K.S. Nahm, IPHE Fuel Cell Cost Comparison Report, International Partnership for Hydrogen and Fuel Cells in the Economy (2008).
[3] B. Ibeh, C. Gardner, M. Ternan, Int. J. Hydrogen Energy 32 (2007) 908–914.
[4] C.L. Gardner, M. Ternan, J. Power Sources 171 (2007) 835–841.
[5] K. Onda, K. Ichihara, M. Nagahama, Y. Minamoto, T. Araki, J. Power Sources 164 (2007) 1–8.
[6] H.K. Lee, H.Y. Choi, K.H. Choi, J.H. Park, T.H. Lee, J. Power Sources 132 (2004) 92–98.
[7] R. Doucet, C. Gardner, M. Ternan, Int. J. Hydrogen Energy 34 (2009) 998–1007.
[8] K. Onda, T. Araki, K. Ichihara, M. Nagahama, J. Power Sources 188 (2009) 1–7.
[9] S.A. Grigoriev, I.G. Shtatniy, P. Millet, V.I. Porembsky, V.N. Fateev, Int. J. Hydrogen Energy 36 (2011) 4148–4155.
[10] M.T. Nguyen, S.A. Grigoriev, A.A. Kalinnikov, A.A. Filippov, P. Millet, V.N. Fateev, J. Appl. Electrochem. 41 (2011) 1033–1042.
[11] K.A. Perry, G.A. Eisman, B.C. Benicewicz, J. Power Sources 177 (2008) 478–484.
[12] M. Thomassen, E. Sheridan, J. Kvello, J. Nat. Gas Sci. Eng. 2 (2010) 229–234.
[13] S.J. Kim, B.-S. Lee, S.H. Ahn, J.Y. Han, H.Y. Park, S.H. Kim, S.J. Yoo, H.-J. Kim, E. Cho, D. Henkensmeier, S.W. Nam, T.-H. Lim, S.-K. Kim, W. Huh, J.H. Jang, Int. J. Hydrogen Energy 38 (2013) 14816–14823.
[14] J.W. Phair, S.P.S. Badwal, Ionics 12 (2006) 103–115.
[15] R.D. Doctor, J.C. Molburg, Hydrogen from steam-methane reforming with CO_2 capture, in: 20th Annual International Pittsburgh Coal Conference, Pittsburgh, PA, 2003.
[16] S. Campanari, J. Power Sources 112 (2002) 273–289.
[17] N. Hoshi, T. Izuwra, Y. Hore, Electrochim. Acta 40 (1995) 883–887.
[18] H. Li, K. Lee, J. Zhang, PEM Fuel Cell Electrocatalysts and Catalyst Layers, 2008, pp. 135–164.
[19] J.K. Nørskov, T. Bligaard, A. Logadottir, J.R. Kitchin, J.G. Chen, S. Pandelov, U. Stimming, J. Electrochem. Soc. 152 (2005) J23.
[20] T.U.N. Hoshi, T. Mizumura, Y. Hori, J. Electroanal. Chem. 381 (1995) 261–264.
[21] N. Hoshi, H. Ito, T. Suzuki, Y. Hori, J. Electroanal. Chem. 395 (1995) 309–312.
[22] M.N.N. Hoshi, T. Suzuki, Y. Hori, J. Electroanal. Chem. 421 (1997) 15–18.
[23] K.S. Lee, S.J. Yoo, D. Ahn, T.Y. Jeon, K.H. Choi, I.S. Park, Y.E. Sung, Langmuir: ACS J. Surf. Colloids 27 (2011) 3128–3137.
[24] M. Hara, K. Asami, K. Hashimoto, T. Masumoto, Electrochim. Acta 28 (1983) 1073–1081.
[25] A. Tanaka, Y. Takeda, M. Imamura, S. Sato, Phys. Rev. B 68 (2003) 195415.
[26] N.K.T. Ioroi, K. Yasuda, Y. Yamamoto, H. Takenakaa, J. Electrochem. Soc. 147 (2000) 2018–2022.
[27] N.M. Markovic, B.N. Grgur, P.N. Ross, J. Phys. Chem. B 101 (1997) 5405–5413.
[28] B.M. Babić, L.M. Vračar, V. Radmilović, N.V. Krstajić, Electrochim. Acta 51 (2006) 3820–3826.
[29] Y. Sun, Y. Dai, Y. Liu, S. Chen, Phys. Chem. Chem. Phys. 14 (2012) 2278–2285.
[30] J. Sobkowski, A.J. Czwrnski, J. Electroanal. Chem. 55 (1974) 391–397.
[31] N. Hoshi, Y. Hori, Electrochim. Acta 45 (2000) 4263–4270.
[32] M.A. Montero, J.L. Fernández, M.R. Gennero de Chialvo, A.C. Chialvo, J. Phys. Chem. C 117 (2013) 25269–25275.